



# Experimental Observations of Gas-sorption-Induced Strain Gradients and their Implications on Permeability Evolution of Shale

Rui Shi<sup>1,2,4</sup> · Jishan Liu<sup>3</sup> · Xiaoming Wang<sup>2</sup> · Derek Elsworth<sup>4</sup> · Zhizhuang Wang<sup>2</sup> · Mingyao Wei<sup>1</sup> · Guanglei Cui<sup>5</sup>

Received: 24 July 2020 / Accepted: 9 April 2021

© The Author(s), under exclusive licence to Springer-Verlag GmbH Austria, part of Springer Nature 2021

## Abstract

Gas adsorption/desorption can result in swelling/shrinking of the matrix in fractured shale. The significant contrast in permeability between fractures and matrix results in an extended duration for the equilibration of the gas injection or depletion-created pressure difference. This spatially non-uniform pressure dissipation induces non-uniform deformations inside the matrix. We follow this response with carefully constrained laboratory measurements integrated with numerical modelling to explore the relation between the strain gradients that develop in the matrix adjacent to fractures and the evolution of permeability each under conditions of constant confining pressure. The microstructures of the sample were characterized by X-ray computed tomography, field-emission scanning electron microscopy and mercury injection capillary pressure porosimetry. A distributed array of strain gauges was attached to the matrix to directly measure the evolving strain. Then a 3D multiphysics numerical model was built to model the evolution of strain gradients from initial to ultimate equilibrium. The influence of these strain gradients on the evolution of fracture permeability is evaluated by a non-uniform strain-based permeability model. The results indicate that the swelling of the matrix near fractures can also compress the matrix away from the fracture under constant confining pressure conditions. Under the influence of the matrix–fracture interaction, a transient and complex distribution of strain gradients develops within the matrix.

**Keyword** Dual porosity · Stress transfer · Swelling strain · Strain gradients · Sorption-induced swelling

## List of Symbols

$b_0$	Initial fracture aperture (m)
$\Delta b$	Fracture aperture change (m)
$f_i$	The component of body force in the $i$ –direction (N)
$E$	Young’s modulus (MPa)

$G$	Shear modulus (MPa)
$K$	Bulk modulus (MPa)
$k_m$	The permeability of matrix system (m <sup>2</sup> )
$k_{m0}$	The initial permeability of matrix system (m <sup>2</sup> )
$k_f$	The permeability of fracture system (m <sup>2</sup> )
$k_{f0}$	The initial permeability of fracture system (m <sup>2</sup> )
$M$	The molecular mass of gas (kg/mol)
$p_m$	The gas pressure in the matrix systems (MPa)
$p_f$	The gas pressure in the fracture systems (MPa)
$p_L$	Langmuir pressure (MPa)
$p$	Pore pressure (MPa)
$R$	The universal gas constant (J/(mol K))
$T$	The absolute gas temperature (K)
$u_i$	The component of displacement in the $i$ -direction (m)
$V_L$	Langmuir volume constant (m <sup>3</sup> /kg)
$\Phi_m$	The porosity of matrix system
$\Phi_f$	The porosity of fracture system
$\bar{\sigma}$	Mean compressive stress (MPa)
$\epsilon_e$	Total effective volumetric strain
$\epsilon_m$	Volumetric strain in the shale matrix
$\epsilon_{mp}$	Effective-stress-induced volumetric strain

✉ Xiaoming Wang  
sunwxm@cug.edu.cn

<sup>1</sup> School of Resources and Geosciences, China University of Mining and Technology, Xuzhou 221116, China

<sup>2</sup> Key Laboratory of Tectonics and Petroleum Resources, Ministry of Education, China University of Geosciences, Wuhan 430074, China

<sup>3</sup> Department of Chemical Engineering, School of Engineering, The University of Western Australia, 35 Stirling Highway, Perth, WA 6009, Australia

<sup>4</sup> Department of Energy and Mineral Engineering, G3 Centre and Energy Institute, The Pennsylvania State University, University Park, PA 16802, USA

<sup>5</sup> Key Laboratory of Ministry of Education on Safe Mining of Deep Metal Mines, Northeastern University, Shenyang 110004, China

$\varepsilon_{ms}$	Sorption-induced volumetric strain
$\varepsilon_f$	Fracture strain
$\varepsilon_f^t$	Uniform strain component
$\varepsilon_f^l$	Non-uniform strain component
$\varepsilon_L$	Langmuir volumetric strain constant
$\nu$	Poisson ratio
$\alpha$	Biot coefficient
$\rho_s$	Shale density (kg/m <sup>3</sup> )
$\rho_a$	Gas density at atmospheric pressure (kg/m <sup>3</sup> )
$\rho_g$	Gas density (kg/m <sup>3</sup> )
$\mu$	Dynamic viscosity of the gas (mPa s)

## 1 Introduction

The recent growth in the utilization of unconventional natural gas is important in the United States (Karacan et al. 2011; Werner et al. 2015) and globally (Wang et al. 2014). Shale gas reservoirs are readily conceptualized as a dual-porosity media that contains a low-permeability high-storage rock matrix transected by a high-permeability low-storage fracture system. However, recent observations indicate that the swelling/shrinking of the matrix system during the adsorption/desorption greatly affects the evolution of permeability (Cui et al. 2018b; Karacan 2007; Kiyama et al. 2011; Pan and Connell 2007). Distinctly contrasting permeabilities of the matrix and fracture systems (Fan et al. 2019; Liu et al. 2020) sustain a pressure difference between the two systems during sorptive gas injection (CO<sub>2</sub> sequestration) or depletion (shale gas extraction). This results in non-uniform deformation within the dual-porosity reservoir and influences the dynamic change of reservoir permeability that ultimately exerts control on gas production during the drainage process (Cui et al. 2018a; Wang et al. 2016; Wei et al. 2019b).

A series of permeability models, based on single/dual poroelastic theory and combined gas slippage effect has been established to account for the experimental observations of shale permeability evolution. These models can be classified into two groups, i.e., stress-dependent (Cui et al. 2018a; Li et al. 2020; Pan et al. 2015b; Tan et al. 2019; Wei et al. 2016, 2019b; Zeng et al. 2020) and stress-independent apparent permeability models (Florence et al. 2007; Klinkenberg 1941). For the stress-independent apparent permeability models, the intrinsic permeability ( $k_{\infty}$ ) is treated as a constant. In addition, the matrix strain should be independent of time during the change of gas pressure. In contrast, for stress-dependent apparent permeability models, under invariant stress conditions, the matrix strain is assumed to be linear with gas pressure at equilibrium conditions.

Permeability experiments comprise three general boundary conditions, representing constant confining pressure (CCP) (Fink et al. 2017; Ghanizadeh et al. 2014; Guo 2014;

Kang et al. 2015; Kumar et al. 2016; Li et al. 2017; Pan et al. 2015b; Ren et al. 2016; Sander et al. 2017; Shen et al. 2018; Zhou et al. 2016, 2020; Zhu et al. 2016), constant effective stress (CES) (Aljamaan et al. 2013; Alnoaimi and Kovscek 2013; Alnoaimi et al. 2014; Cui et al. 2010; Firouzi et al. 2014; Gao and Yu 2018; Heller et al. 2014; Jin et al. 2015; Letham 2011; Moghadam and Chalaturnyk 2015, 2016; Moghaddam and Jamiolahmady 2016; Pan et al. 2015b; Peng and Loucks 2016; Zamirian et al. 2014a; Zhu et al. 2016), and constant pore pressure tests (Chen et al. 2019; Chen et al. 2020; Ghanizadeh et al. 2014; Ma et al. 2016; McKernan et al. 2014; Pan et al. 2015a; Peng and Loucks 2016; Tan et al. 2017, 2018; van Noort and Yarushina 2019; Wang et al. 2019; Zamirian et al. 2014b; Zhou et al. 2016, 2019). These are generally completed to study the mechanistic properties of gas transport in shale samples. Regardless of the boundary conditions, the pressure difference between the matrix system and the fracture system is typically ignored in these experiments—and steady conditions assumed in the interpretation of the results (Shi et al. 2018). An implicit assumption of equilibrium between matrix and fractures is adopted when permeability is measured (He et al. 2020). Unfortunately, few direct observations of the non-uniform matrix strain are available when a pressure difference (pressure gradient) exists between the matrix and fractures, and the distribution of deformations in different parts of the sample has not been fully understood.

The following study reports the results of the time history of the strain gradients through a fractured sample using the proxy of measured strains. A series of strain gauges measure transient stress/strain transfer between matrix and fracture and record deformations at different proximities to a control fracture for unconstrained deformation boundary conditions (constant macroscopic stress). Multiple microscopic characterization techniques, including X-ray CT imaging, field-emission scanning electron microscopy (FE-SEM), and mercury injection capillary pressure porosimetry (MICP), are used to define fundamental microstructural characteristics of the sample matrix and transecting fractures. This work offers a direct observation of the transient strain gradients in the matrix under the influence of the matrix–fracture interactions.

## 2 Experimental Methods

A prismatic fractured shale sample was used to measure the gas sorption (methane) induced transient evolution of strain gradients at the decimeter scale under free swelling conditions. X-ray CT imaging characterizes the fracture distribution within the sample and mercury injection capillary pressure porosimetry (MICP) defines the pre-sorption pore throat size distribution. Surface-mounted strain gauges were

attached to the sample to monitor the evolution of the local linear strains at different locations relative to the fracture.

## 2.1 Sample Information

Outcrop shale samples collected from the Lower Silurian Longmaxi Formation of the Sichuan Basin, China, are used in the experiments with basic information obtained from X-ray CT imaging, FE-SEM, and MICP tests.

### 2.1.1 Sample Preparation

Prismatic blocks of outcrop shales (TOC (total organic carbon) content is 5.45%) used in the deformation experiments were collected from the Lower Silurian Longmaxi Formation, Sichuan Basin, China. Then a single prismatic sample was cut from the larger prismatic blocks for the deformation tests—containing a fracture (light green shaded area) that was cut on one side of the sample, as shown in Fig. 1. The horizontal-*X* and horizontal-*Y* directions are parallel to the bedding layers, and the vertical-*Z* direction is perpendicular to the bedding layers. The height of the sample is  $\sim 9$  cm, and the length and width are each  $\sim 3.5$  cm. The aperture of the fracture is  $\sim 1.15$  mm. The sample was dried at  $50^\circ\text{C}$  for 48 h to remove moisture before the experiments.

### 2.1.2 X-ray CT Imaging

The interior three-dimensional structure of the sample was imaged via X-ray computed tomography (CT) (Wildenschild and Sheppard 2013). A Nanotom X-ray computed

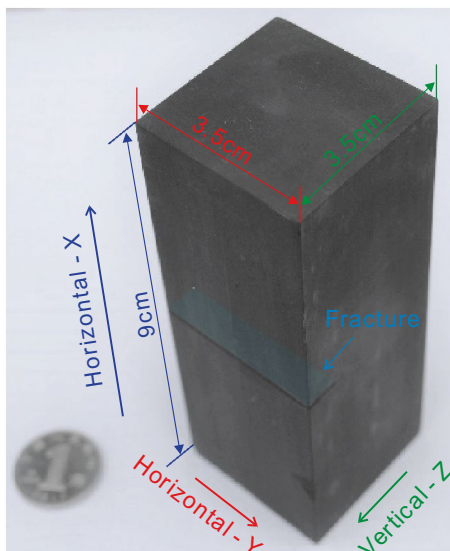


**Fig. 1** Shale sample showing dimensions and location of cut fracture (horizontal—the direction parallel to the bedding layers)

tomography instrument from GE Phoenix was used to scan the prismatic sample at a resolution of  $1\ \mu\text{m}$ . The sample was dried at  $50^\circ\text{C}$  for 48 h to remove moisture.

### 2.1.3 Field Emission Scanning Electron Microscopy (FE-SEM)

One surface of the small sample ( $\sim 1\ \text{cm} \times 1\ \text{cm} \times 0.35\ \text{cm}$ ) that was cut from the shale blocks during processing was selected and polished by argon-ion milling to create a smooth surface using a Hitachi Ion Milling System IM4000. The small sample was dried at  $60^\circ\text{C}$  for 48 h to remove moisture. A 10-nm-thick layer of gold was coated on the shale surface to enhance the electrical conductivity to obtain both microstructure and morphology using field emission scanning electron microscopy (FE-SEM) (instrument: Quanta 450).

### 2.1.4 Mercury Injection Capillary Pressure Porosimetry (MICP)

The pore size distribution of the sample was characterized by Mercury Injection Porosimetry (instrument: Micromeritics AutoPore IV9510). This apparatus acquires the characteristics of the porosity distribution and the connectedness of that porosity for the nano-scale pore system (Yang and Liu 2019). The experiments were performed on a cubic sample (size  $\sim 1 \times 1 \times 1\ \text{cm}^3$ ) following drying at  $60^\circ\text{C}$  for 48 h to remove moisture. The pore-throat diameter distribution is directly obtained using the Washburn equation (Washburn 1921), assuming a surface tension of  $485\ \text{mN/m}$  and a contact angle of  $130^\circ$  (Gan et al. 1972) for the intruding mercury.

## 2.2 Experimental Set-Up

As shown in Fig. 2, the apparatus comprises three parts, i.e., a thermostatic chamber, the gas pressure system, and the data acquisition system. The experimental set-up was designed to enable the measurement of strain induced by gas adsorption (Liu and Harpalani 2014; Shi et al. 2020). The high-pressure vessel is placed in a thermostatic chamber, which can maintain a constant temperature during the entire experiment. The gas pressure is controlled by a gas pressure controller and monitored by a pressure transducer. Evolving strains in the sample are collected by a data acquisition system.

## 2.3 Experimental Procedure

As shown in Fig. 3, a series of strain gauges was attached to the surface of the sample to measure the deformation history of the shale, directly and in a specific orientation

**Fig. 2** Schematic of the experimental apparatus used to measure the strain of the sample (after Shi et al. 2020)

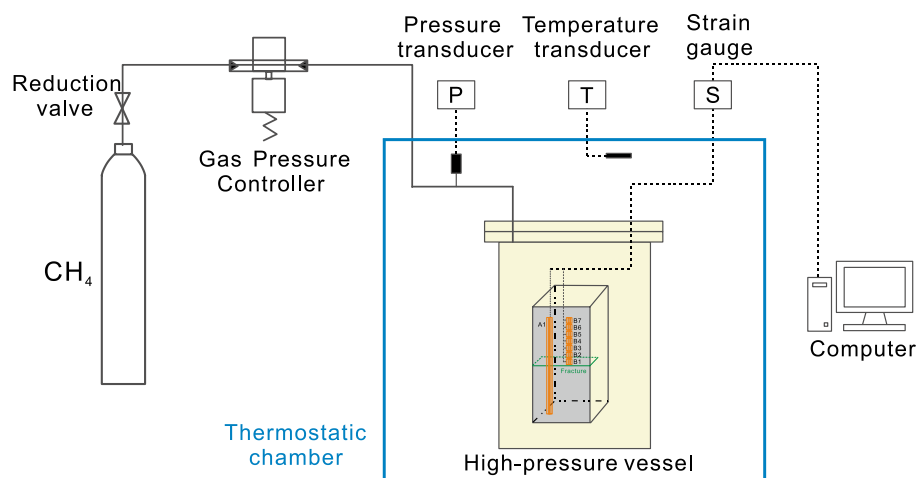
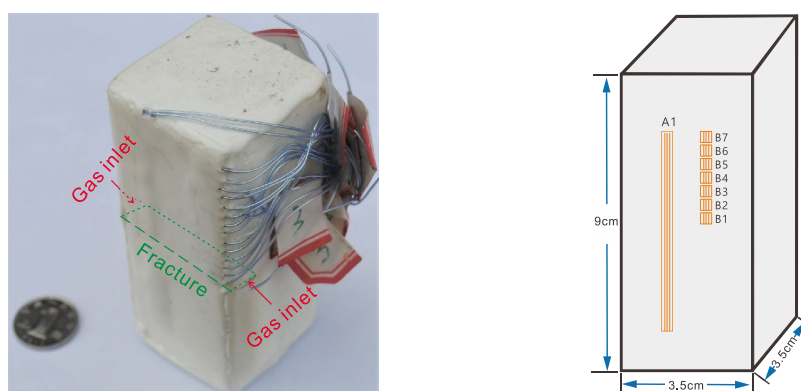


**Fig. 3** Schematic of the sample with strain gauges



**(a)** Shale sample with silicone rubber jacket. **(b)** Schematic of strain gauge locations.

(Liu and Harpalani 2013). These observations are used to understand the coupling between deformation and dynamic gas injection (Kiyama et al. 2011; Liu et al. 2016). They were designed to measure the sorption-induced strain in the horizontal direction on the designated surface (Sang et al. 2017). The average deformation of the entire sample was measured by strain gauge A1. To further record the deformation data in different parts of the sample at different distances from the fracture, a series of strain gauges (B1–B7) was applied on the sample, as shown in Fig. 3b. From the bottom to top, the strain gauges are B1, B2, B3, B4, B5, B6 and B7, respectively. Following the attachment of the gauges, the entire sample was encased in a layer of soft silicone rubber adhesive to ensure that the gas can only infiltrate the sample through the two ends of the fracture, as shown in Fig. 3a. Then the entire assembly was placed in a high-pressure vessel (Fig. 2). After reaching the designed temperature (maintained at 35°C), the gas pressure was increased from 0 to 1.0 MPa at a rate of 0.2 MPa/10 s and then held constant at 1.0 MPa.

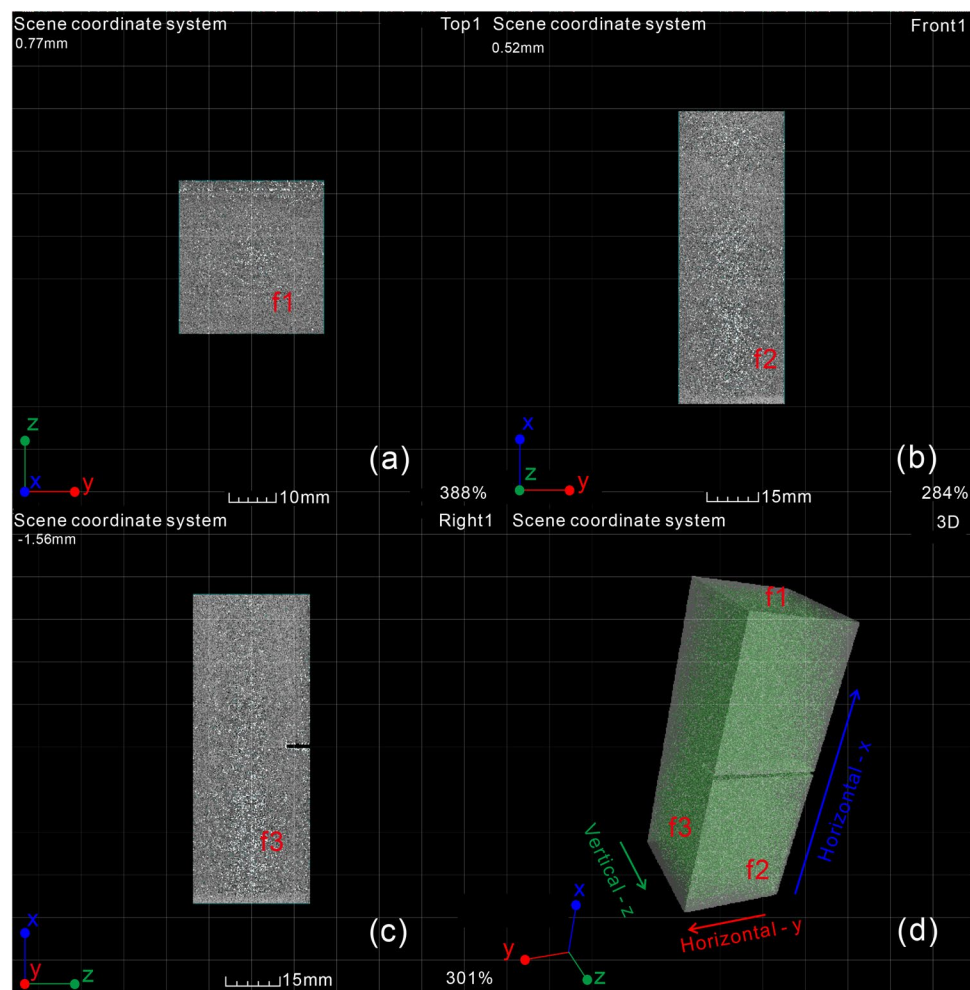
### 3 Experimental Results and Discussion

The dynamic experiments performed on the characterized shale samples involve adsorption and measurement of the active generation of surface linear strain gradients. The microstructures of the shale matrix and fractures were characterized by X-ray CT imaging, FE-SEM, and MICP techniques. The evolutions of the surface linear strain distributions were directly observed by the strain gauges.

#### 3.1 Description of Fracture System by X-ray CT Imaging

Shale is a dual-porosity system comprising matrix and fractures. From the CT imaging (Fig. 4), no obvious millimeter-scale fractures were identified in the characterized sample, except for the artificial fracture on one side of the sample. The artificial fracture on face f2 is mostly in the horizontal(-X) direction. The distribution of aperture

**Fig. 4** CT radiographs of the shale sample showing different faces: **a** f1, **b** f2, **c** f3, and **d** a three-dimensional view of the shale sample



within the fracture appears uniform, with an aperture of  $\sim 1.15$  mm.

### 3.2 Description of Matrix System by X-ray CT Imaging, FE-SEM, and MICP Tests

X-ray CT imaging, FE-SEM, and MICP tests were used to record information on pore structure and the microfractures transecting the matrix system. From Fig. 4, a large number of micron-scale pores are observed in the X-ray CT imaging results of the prismatic shale sample. The microfractures in the matrix system were observed by FE-SEM, and the results are shown in Fig. 5a–d. Microfracture 1 in Fig. 5a is filled with pyrite and organic matter and shows a largely uniform aperture that is of the order of  $\sim 50$   $\mu\text{m}$ . Microfracture 2 is relatively tortuous with a non-uniform aperture ranging from  $\sim 0.5$  to  $\sim 5$   $\mu\text{m}$  (Fig. 5b). The microfracture 3 is surrounded by clusters of organic pores, quartz, and pyrite with a relatively tortuous topology (Fig. 5c). In contrast, no microfractures can be identified in some areas, as in Fig. 5d. The results illuminate that the distribution of microfractures

in the matrix system is complicated, which indicates a relatively strong heterogeneity in the shale matrix.

The pore size distribution is presented in Fig. 6 (Gallé 2001). With an increase in applied pressure, a significant volume of mercury intrudes into the connected pores in the shale sample, suggesting that the sizes of some pores are in the meso-macropore range. The average pore throat size, indexed by 50% volume of the shale sample, is less than 10 nm, which denotes a relatively low permeability for the connected nano-scale pore network (Hu et al. 2015; Katz and Thompson 1986).

### 3.3 Changes of Shale Linear Strain with Time

The strain gauges cannot be attached to the fracture void; thus it is difficult to directly measure the compression across this section. Figure 7 presents the evolution of the linear strains in the shale with time during the injection of an adsorptive gas ( $\text{CH}_4$ ). Strain gauge A1 records the deformation of the entire sample and strain gauges B1–B7 record the deformation in different parts of the sample at different

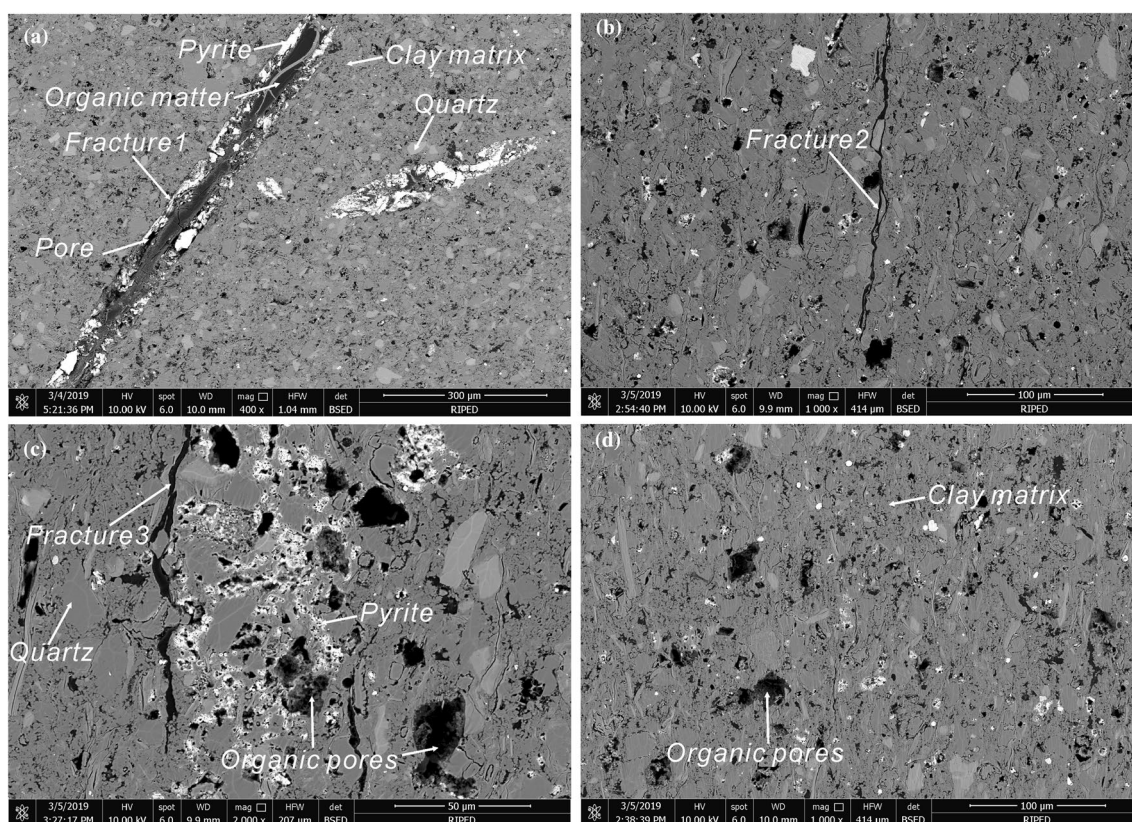


**Fig. 5** FE-SEM images of the shale samples. **a** microfracture 1—filled with pyrite and organic matter; **b** microfracture 2—with a relatively tortuous topology; **c** microfracture 3—surrounded by organic pores, quartz, and pyrite; **d** matrix containing no obvious microfractures

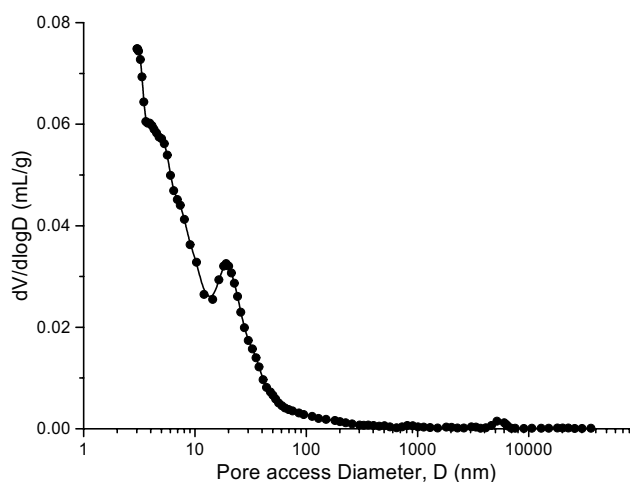


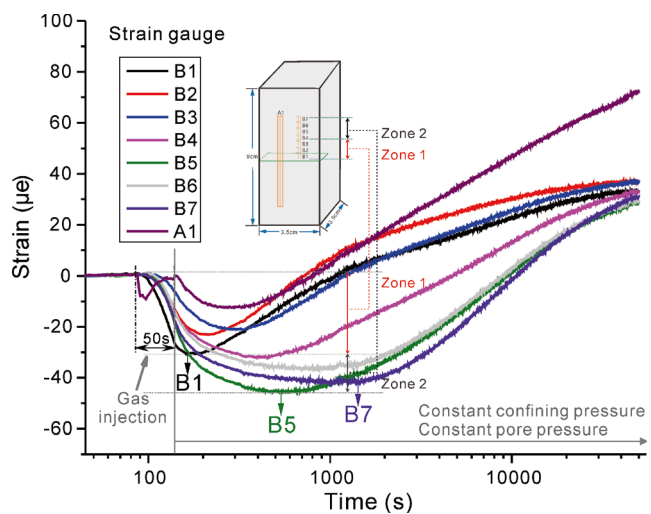
**Fig. 6**  $dV/d\log D$  versus pore diameter from mercury intrusion showing pore size distribution for the shale sample

distances from the fracture. In this paper, positive strain denotes extension and negative strain denotes compression. The evolution of strains with time can be divided into three stages that exhibit similar trends. First, shale linear strains decrease gradually following the initiation of gas injection.

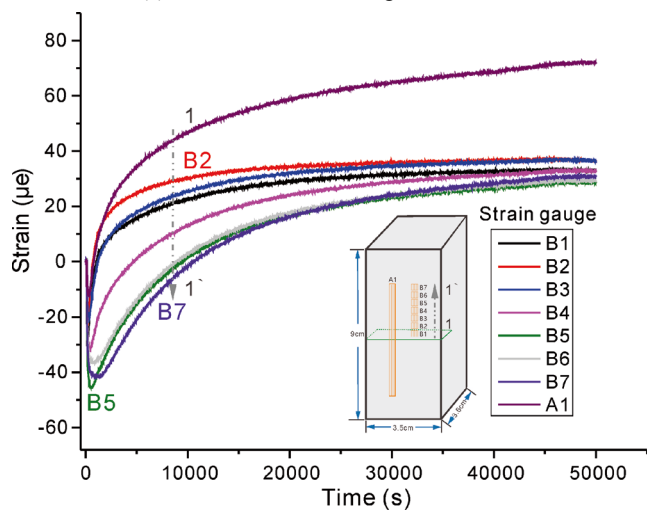
When the gas pressure is held constant at 1.0 MPa, shale linear strains continue to gradually decrease with time until they reach a minimum. The differences between the various responses are in terms of rate and magnitude. Next, the shale linear strains begin to gradually increase and finally reach a plateau. In the whole process, the maximum contractive linear strain was of the order of  $45.5\mu\epsilon$ , and the maximum swelling linear strain was  $\sim 69.6\mu\epsilon$ .

The time to reach the minimum linear strain and the magnitude of the minimum linear strain is closely related to the distances of the strain gauges from the fracture. Strain gauge B1 is the closest to the fracture and the earliest to reach the minimum. The time to reach the minimum linear strain increases gradually with an increase of the distances from the strain gauges to the fracture. At the early time ( $t < 2000s$ ), the deformation can apparently be divided into two zones (zones 1 and 2 in Fig. 7a). Zone 1 represents the measured results of strain gauges B1-4 (red arrow in Fig. 7a) and the magnitude of the minimum linear strain is relatively small, while the magnitude of the minimum linear strain is relatively large in zone 2 (strain gauges B5-7, black double arrow in Fig. 7a). After the initial stage ( $t > 2000s$ ), the magnitude of the swelling strain decreases with an increase in the distance from the strain gauges to the fracture (grey

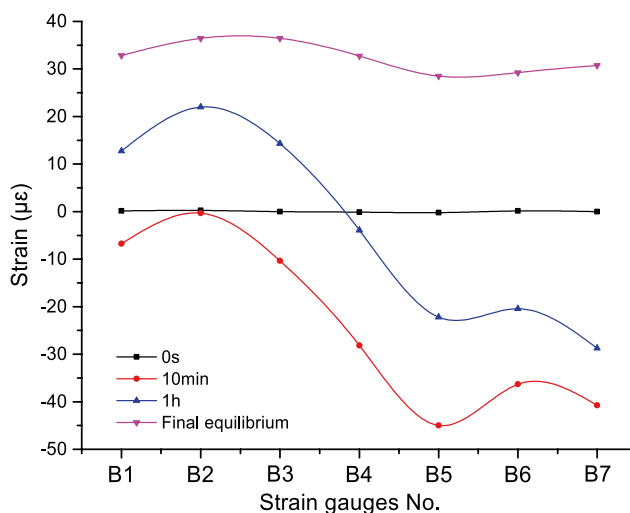
**Fig. 7** Evolution of measured strains during injection of CH<sub>4</sub>



(a) Strain evolution with logarithmic time.



(b) Strain evolution with time.



(c) Strain evolution with distance to the fracture at different times after gas injection.

dotted arrow in Fig. 7b). These results show the evolution rates and magnitudes of the different average matrix strains in different parts of the sample. For the strain gauges near the fracture (strain gauges B1-4), the equilibrium time is shorter than that for the strain gauges distant from the fracture (strain gauges B5-7), while the magnitude of shrinkage in the proximal measurements is larger than those more distant (strain gauges B5-7). The swelling/shrinkage of the shale matrix–fracture interactions is a transient process and transient deformation gradients develop as a result in the shale matrix (Fig. 7c), which have not been taken into consideration in most permeability models. The interactions between the matrix and the fracture are caused when gas is injected into the sample, gas rapidly invades the fracture due to its relatively high permeability, leading to a pressure difference between the matrix and the fracture. Next, with the gas contacting the fracture surface and diffusing into the matrix, the deformation of the matrix and the deformation of the fracture will continue to influence each other (Shi et al. 2018). To further understand these intrinsic interaction mechanisms, we constructed a numerical model to analyze the experimental results.

## 4 Theory and Modeling

In the following, a multiphysics-based numerical model was built to model the evolution of strain gradients from initial to ultimate equilibrium. The mechanisms of gas sorption-induced strain gradients under the influence of matrix–fracture interactions were analyzed. Furthermore, the influence of these strain gradients on the evolution of fracture permeability is evaluated by applying the non-uniform strain history into a permeability model.

### 4.1 Governing Equations of Shale Deformation

It is assumed that both the fracture and the matrix are homogeneous and elastic and that the deformation obeys Hooke’s law. Based on previous work (Wu et al. 2010; Zhang et al. 2008), both in the matrix and the fracture regions the deformation can be described as

$$Gu_{i,kk} + \frac{G}{1-2\nu}u_{k,ik} - \alpha p - K\varepsilon_L \frac{p_L}{(p+p_L)^2}p_i + f_i = 0 \quad (1)$$

where  $G$  is the shear modulus with  $G = E / 2(1 + \nu)$ ,  $u_i$  is the component of displacement in the  $i$ -direction,  $\nu$  is the Poisson ratio,  $\alpha$  is the Biot coefficient,  $p$  is the pore pressure,  $E$  is Young’s modulus,  $K$  is the bulk modulus with  $K = E / 3(1 - 2\nu)$ ,  $\varepsilon_L$  is the Langmuir volumetric strain constant (in the matrix region),  $p_L$  is the Langmuir pressure (in the matrix region), and  $f_i$  is the component of body force in

the  $i$ -direction. Besides, the subscripts “ $f$ ” and “ $m$ ” denote the properties of fractures and rock matrix, respectively. For example,  $E_f$  is Young’s modulus of the fractures, and  $E_m$  is Young’s modulus of the matrix.

### 4.2 Mass Balance Equation

(1) Governing equation for gas flow within the matrix.

The governing equation for matrix for the ideal absorbing gas is (Wei et al. 2019a):

$$\frac{d}{dt} \left( \phi_m p_m \frac{M}{RT} + (1 - \phi_m) \rho_s \rho_a \frac{V_L p_m}{p_m + P_L} \right) - \nabla \cdot \left( \rho_g \frac{k_m}{\mu} \nabla p_m \right) = Q_s \quad (2)$$

where  $\phi_m$  is the porosity of the matrix system,  $M$  is the molecular mass of gas,  $T$  is the absolute gas temperature,  $R$  is the universal gas constant,  $p_m$  is the gas pressure in the matrix,  $\rho_s$  is shale density,  $\rho_a$  is the gas density at atmospheric pressure,  $V_L$  is the constant of Langmuir volume,  $\rho_g$  is the gas density,  $\mu$  is the dynamic viscosity of the gas,  $k_m$  is the matrix permeability, and  $Q_s$  is the gas source or sink. Under the stress-controlled boundary conditions used here, the porosity of the matrix is related to the effective volumetric strain (Liu et al. 2010) and the matrix porosity change can be expressed as

$$\frac{\phi_m}{\phi_{m0}} = 1 + \frac{\alpha}{\phi_{m0}} \Delta \varepsilon_{me} \quad (3)$$

where  $\Delta \varepsilon_{me}$  is the total effective volumetric strain and  $\Delta \varepsilon_{me} = -(\bar{\sigma} - \alpha_f p_f - \alpha_m p_m) / K_m$ ,  $\bar{\sigma} = \sigma_{kk} / 3$  is the mean compressive stress. Here we use a simple approach to estimate the influence of the change of porosity during matrix deformation on the evolution of shale matrix permeability. The permeability change can be calculated through the change in porosity (Liu et al. 2011; Zhang et al. 2008) and thus the permeability change for the shale matrix system can also be expressed as

$$\frac{k_m}{k_{m0}} = \left( \frac{\phi_m}{\phi_{m0}} \right)^3 = \left( 1 - \frac{1}{\phi_{m0}} \frac{\bar{\sigma} - \alpha_f p_f - \alpha_m p_m}{K_m} \right)^3 \quad (4)$$

(2) Governing equation for gas flow within fractures.

The governing equation for mass conservation represents gas transfer through the fractures and simplifies to a pressure boundary on the matrix–fracture interface due to the extremely fast equilibration (Liu et al. 2018). Then the pore pressure ( $p_f$ ) is assumed to be increased gradually within the 50 s from the initial application of pore pressure  $p_{m0}$

(0.1 MPa) to a constant pore pressure  $p_l$  (1.0 MPa) and defined as

$$p_f = \begin{cases} p_l & t \geq 50s \\ t * 0.018 * p_l + p_{m0} & t < 50s \end{cases} \quad (5)$$

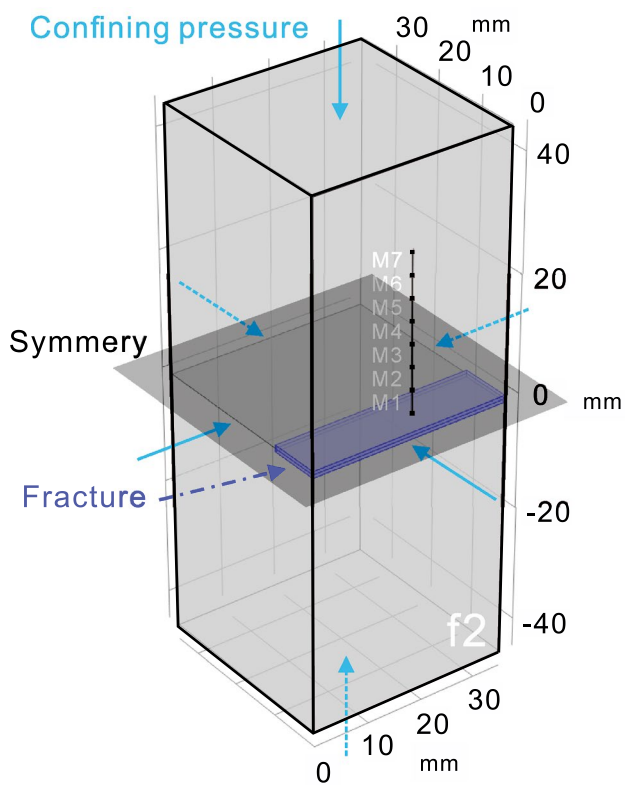


Fig. 8 Geometry of the 3D symmetric model with boundary conditions

For a single fracture, the fracture permeability is defined as (Lomize 1951)  $k_f = b^2/12$ , where  $k_f$  is the fracture permeability of the sample,  $b$  is the fracture aperture. This is an analytical result (not empirical) based on the flow between parallel plates. Then the fracture ratio can be expressed as

$$\frac{k_f}{k_{f0}} = \left(\frac{b}{b_0}\right)^2 = \left(1 + \frac{\Delta b}{b_0}\right)^2, \quad (6)$$

where  $k_{f0}$  is the initial fracture permeability of the sample,  $\Delta b$  is the fracture aperture change, and  $b_0$  is the initial fracture aperture.

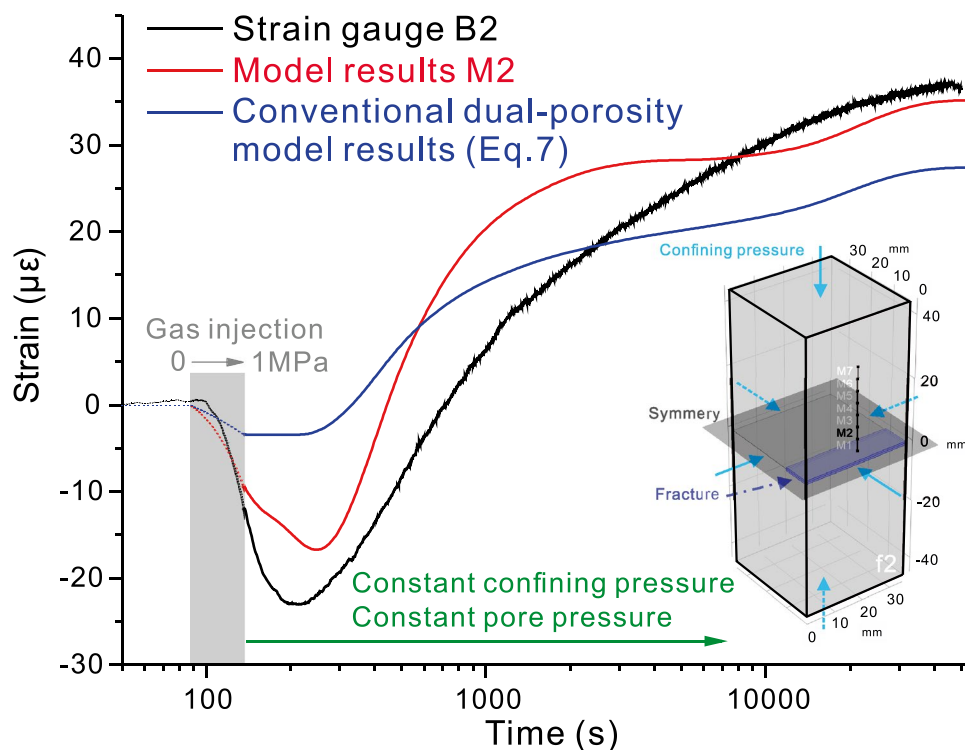
### 4.3 Model Implementation and Validation

The sample is a 3D rectangular numerical model (90 mm × 35 mm × 35 mm), as described in Fig. 8. The principal fracture is present on one side of the sample with an aperture of 1.15 mm. Injection of methane (CH<sub>4</sub>) is taken as one possible condition to drive the evolution of linear strain gradients within the shale matrix at constant confining pressure. All external boundaries are applied with no flow conditions and the mass exchange between the matrix and fracture occurs on the connecting boundary. The matrix and fracture domains are connected by a pressure continuity interface boundary across the interior boundary (Wei et al. 2019a). The applied pore pressure and confining pressure increase from 0 to 1.0 MPa at a rate of 0.2 MPa/10 s, then remain constant at 1.0 MPa. The properties of the fractures and matrix system are listed in Table 1. The modelling results identify that the evolutions

Table 1 Modelling parameters

Parameters	Value	Source
Young's modulus of matrix, $E_m$	35 GPa	Modified according to Li et al. (2020)
Young's modulus of fracture, $E_f$	0.5 GPa	Modified according to Liu et al. (2018)
Langmuir volume of matrix, $V_L$	0.017 m <sup>3</sup> /kg	Modified according to Li et al. (2020)
Langmuir pressure of matrix, $p_L$	3 MPa	Li et al. (2020)
Langmuir volumetric strain, $\epsilon_L$	0.0003	Modified according to Li et al. (2020)
Poisson ratio of matrix, $\nu_m$	0.3	Modified according to Li et al. (2020)
Poisson ratio of fracture, $\nu_f$	0.3	Modified according to Li et al. 2020
Biot coefficient of matrix, $\alpha_m$	0.4	Modified according to Li et al. (2020)
Biot coefficient of fracture, $\alpha_f$	0.6	Modified according to Li et al. (2020)
Shale density, $\rho_s$	2600 kg/m <sup>3</sup>	Modified according to Li et al. (2020)
Gas viscosity, $\mu$	1.84 × 10 <sup>-5</sup> Pa·s	Constant
Initial porosity of matrix, $\phi_{m0}$	0.02	Modified according to Li et al. (2020)
Initial matrix permeability, $k_{m0}$	2.5 × 10 <sup>-18</sup> m <sup>2</sup>	Modified according to Li et al. (2020)
Initial fracture aperture, $b_0$	1.15 mm	Experimental test
Injection pressure, $p_l$	1 MPa	Experimental setting

**Fig. 9** Comparison among experimental observations and model and numerical results



of the strain is in good agreement with the laboratory results measured by strain gauges B2 (Fig. 9).

#### 4.4 Analysis of the Transient Deformation Gradients

Figure 10 presents the modelling results of the transient evolution of linear strains within the shale, the  $M_i$  in Fig. 10 is corresponding to the strain gauge  $B_i$  in Fig. 7. The results can be divided into four different parts. From top to bottom, these four parts are (a) evolution of swelling area (linear strain  $> 1\mu\epsilon$ ) at different times, (b) evolution of linear strain at different times, (c) evolution of average linear strain magnitude at locations  $M_1$ – $M_7$ , respectively, and (d) distribution of linear strain magnitude with distance to the fracture at location  $M_1$ – $M_7$  at different times. Four representative times are chosen for analysis and these are 0 s before gas injection, 600 s (10 min) after the initiation of gas injection, 3600 s (1 h) after gas injection, and the final equilibrium time.

Prior to injection, the sample is at stress equilibrium and the linear strain is set to be equal to 0. This is treated as the initial state. Under this condition, no swelling occurs at any part of the sample, as shown in Fig. 10a(0 s), b(0 s), c(1–1' red point), and d (1–1' solid line). Then the applied confining pressure and pore pressure increase gradually from 0 to 1.0 MPa and are then held constant at 1.0 MPa. During the increase in confining pressure and pore pressure, the shrinkage in  $M_1$ – $M_7$  for the entire sample decrease with an increase in time due to the influence of the Biot coefficient not being

1 (when confining pressure and pore pressure increase to the same magnitude, the applied effective stress continues to increase) and the time delay for the equilibration of pore pressure in the matrix system ( $p_m < p_f$ ). Then the confining pressure is held constant at 1.0 MPa, and the pore pressure in the matrix begins to increase as the gas diffuses from the fracture to the matrix. As shown in Fig. 10a (10 min), b (10 min), c (2–2' red points line), and d (2–2' dash dot line), after 10 min of gas injection, the matrix adjacent to the fracture swells, while the matrix distant from the fracture shrinks. At 10 min, the largest swelling strain is adjacent to the fracture, while the largest shrinkage strain is in the central area (redpoint 2' on  $M_4$ ,  $y = 17$  mm) between the fracture and the sample boundary, as shown in Fig. 10 c and d (2–2' dash dot line). Then the swelling zone widens with the gas diffusing further into the matrix, as shown in Fig. 10a (1 h), b (1 h), c (3–3' red points line), and d (3–3' dot line). Under this condition, the largest swelling strain is adjacent to the fracture (redpoint 3 on  $M_1$ ), while the largest shrinkage strain is adjacent to the sample boundary (redpoint 3' on  $M_7$ ), as shown in Fig. 10c, d (3–3' dot line). As the gas pressure front propagates throughout the matrix, a new equilibrium state between the matrix and the fracture is established, as shown in Fig. 10a (final equilibrium), b (final equilibrium), c (4–4' red points line), and d (4–4' dash line).

Compared with the experimental observations (Fig. 7a), the evolution of numerical results in Fig. 10c shows a strict relationship with the relationship to the distance to the

fracture, while the experimental observations show that deformation can be divided into two zones. This discrepancy may be caused by the heterogeneity of the sample, as depicted in Fig. 5 showing the FE-SEM images. The time to reach the minimum linear strain is closely related to the distances from the fracture and both can be observed in the experimental observation and the numerical results. Moreover, the time to reach the minimum linear strain prolongs with an increase in the distances from the fracture.

#### 4.5 Distribution of Matrix Strain Under the Influence of Matrix–Fracture Interactions

The experimental results (Fig. 7c) indicate transient strain gradients. But in conventional dual-porosity models, the interactions between matrix and fractures are normally characterized through two equilibrium systems within the same REV (representative elementary volume) (Wei et al. 2021). The matrix pore pressure within each REV is assumed to be uniform (Sang et al. 2016; Wu et al. 2010; Wei et al. 2021). Therefore, in conventional dual-porosity models it is also assumed that the matrix strain within the REV is uniform at any given time and thus the matrix strain gradient must be zero. Here we use the conventional dual-porosity model to study how the matrix strain evolves over time without the influence of the interaction between the matrix and the fracture.

Volumetric strain in the shale matrix is defined as (Zhang et al. 2008):

$$\epsilon_m = \epsilon_{mp} + \epsilon_{ms} \tag{7}$$

where  $\epsilon_m$  is the volumetric strain in the shale matrix,  $\epsilon_{mp}$  is the change in effective-stress-induced volumetric strain, and  $\epsilon_{ms}$  is the sorption-induced volumetric strain. In conventional dual-porosity models (Wei et al. 2021; Wu et al. 2010), the change in effective-stress-induced volumetric strain is described as

$$\epsilon_{mp} = -\frac{1}{K_m} (\bar{\sigma} - \alpha_f p_f - \alpha_m p_m) \tag{8}$$

And the volumetric strain  $\epsilon_{ms}$  can be expressed as (Wu et al. 2011; Zhang et al. 2008):

$$\epsilon_{ms} = \epsilon_L \frac{p_m}{p_L + p_m} \tag{9}$$

Figure 9 (blue line, numerical results, Eq. 7) presents the strain evolution with time without the influence of matrix–fracture interaction as evaluated in a conventional dual-porosity model. The gas pressure simulated at M2 (on the midline of face f2, which is perpendicular to the fracture, as shown in Figs. 8, 9) is used here as the average matrix pore pressure for the uniform calculations. As shown in Fig. 9, when the applied pore pressure and the

confining pressure are constant (green arrow), the strains in both the modelling results M2 (Sect. 4.3) and the experimental results continue to gradually decrease (compression) with time until they reach a minimum. While in the numerical results from the conventional dual-porosity model, the strain begins to gradually increase and finally asymptotes to a constant magnitude. As assumed in many experiments and permeability models (Aljamaan et al. 2013; Alnoaimi and Kovscek 2013; Liu et al. 2011; Zhao et al. 2019), the swelling of the matrix will cause compaction and narrowing of the fracture. Here it is observed that this swelling will also induce transient shrinkage in the matrix that is distant from the fracture, as shown in Figs. 9 and 10. In conventional dual-porosity models, this important interaction between the matrix and the fracture is not considered—neglecting a physically important observed interaction. In conventional dual-porosity models, it is generally assumed that the matrix strain within the REV is uniform but changes in time—thus the matrix strain gradient should be zero. Conversely, in Figs. 7c and 10d, the matrix strain gradients are non-zero and shown to evolve in both space and in time; therefore, the behavior apparent in existing equilibrium-assumption permeability models does not match with observations from laboratory experiments in the period prior to attaining the full equilibrium condition. This correction to represent real behavior seems important.

#### 4.6 A Non-Uniform Strain-Based Permeability Model

The influence of the strain gradients on the evolution of fracture permeability may be evaluated from our permeability model. Based on the fundamental tenets of poroelasticity, the fracture permeability can be defined as a function of effective strain (Liu et al. 2011; Wei et al. 2019a; Zhang et al. 2008) as

$$\frac{k_f}{k_{f0}} = \left( \frac{\phi_f}{\phi_{f0}} \right)^3 = \left( 1 + \frac{\alpha_f}{\phi_{f0}} \Delta \epsilon_e \right)^3 = \left( 1 + \frac{\alpha_f}{\phi_{f0}} \left( \Delta \epsilon_f - \frac{p_f}{K_m} \right) \right)^3 \tag{10}$$

where  $\Delta \epsilon_e$  is defined as the total effective volumetric strain,  $\phi_f$  is the porosity of the fracture system,  $\phi_{f0}$  is the initial porosity of the fracture system,  $\epsilon_f$  is the fracture strain. The fracture strain is dependent on the interactions between fracture and matrix. As shown in Fig. 10c, the distribution of the strain in the matrix changes with time and the effect of non-uniform deformation on fracture permeability is dependent on the strain difference adjacent to fracture. Thus the fracture strain is composed of two components: the uniform strain component which is induced by the uniform fracture deformation, and the non-uniform strain component which is induced by the strain variation within the matrix, as shown

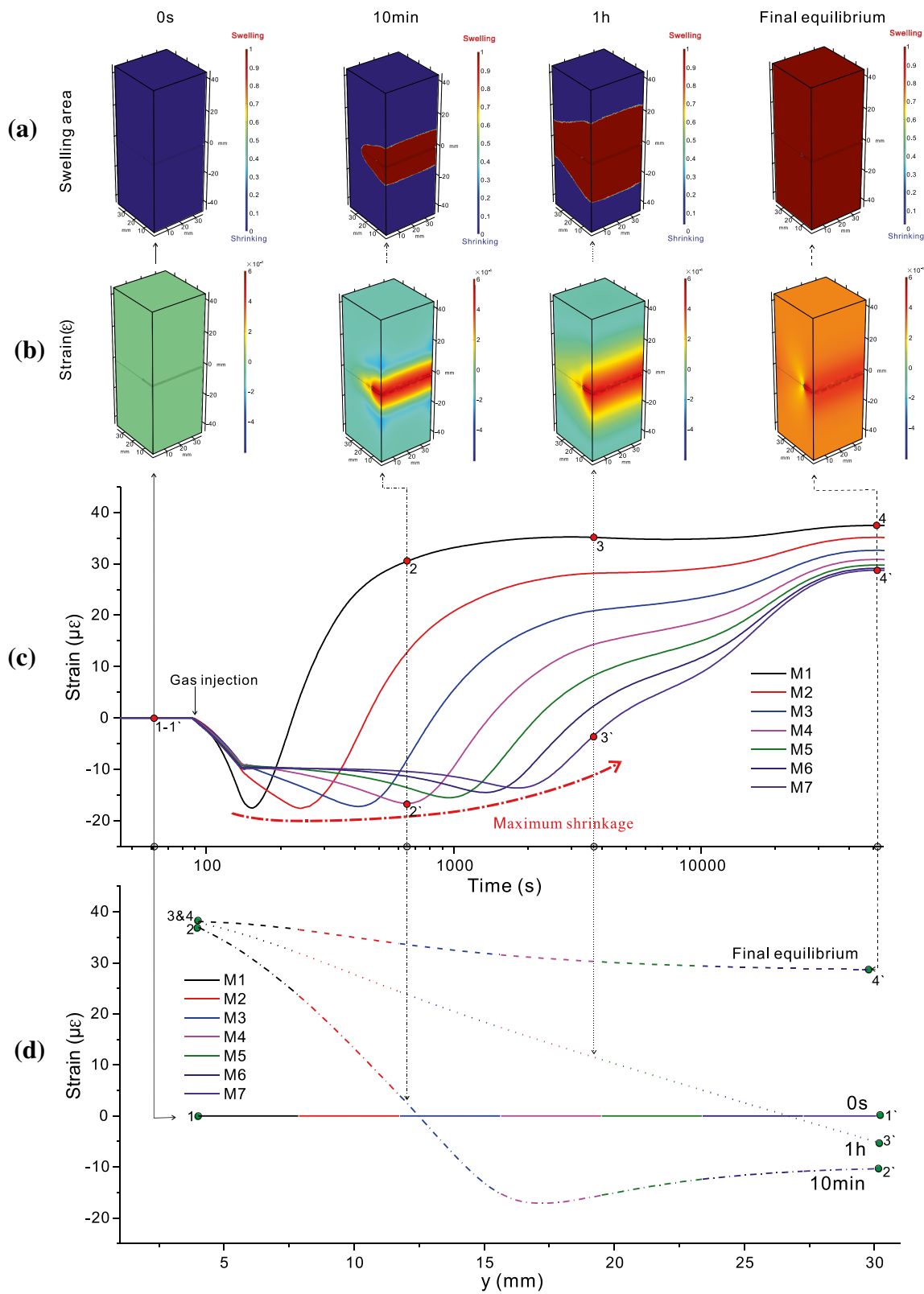


**Fig. 10** Evolution of modeled strains at reference locations with time during injection of CH<sub>4</sub>. **a** Evolution of swelling area (linear strain > 1με) at different times, **b** evolution of linear strain at different times, **c** evolution of average linear strain magnitude at locations M1–M7, respectively, and **d** Distribution of linear strain magnitude with distance to the fracture at location M1–M7 at different times

in Fig. 11. “Non-uniform strain” is caused when there is a pressure difference between the matrix and the fracture; it takes a significant time for gas transport to penetrate into the matrix, leading to a nonuniformity in the gas pressure distribution and hence the distribution of swelling strain in the matrix (Wei et al. 2019a). Thus, the total fracture strain is defined as

$$\Delta \epsilon_f = \Delta \epsilon_f^t + \Delta \epsilon_f' \tag{11}$$

where  $\epsilon_f$  is the fracture strain,  $\epsilon_f^t$  is the uniform strain component,  $\epsilon_f'$  is the non-uniform strain component.

The total fracture strain is defined as (Liu et al. 2011).

$$\Delta \epsilon_f^t = -\frac{1}{K_f} (\Delta \bar{\sigma} - \alpha_f \Delta p_f) \tag{12}$$

In this study, we use the strain difference in different parts of the matrix: one is proximal to the fracture and the other is distal from the fracture and these are used to characterize this non-uniform strain component, as shown in Fig. 11 (Wei et al. 2019a). Then the non-uniform strain component is expressed as

$$\Delta \epsilon_f' = \Delta \epsilon_{mb} - \Delta \epsilon_{ma} \tag{13}$$

where  $\epsilon_{mb}$  is the matrix strain near the fracture, and  $\epsilon_{ma}$  is the matrix strain distant from the fracture. The assumption here is that the non-uniform strain component can be considered as the strain difference in the matrix. Substituting Eqs. (11)–(13) into Eq. (10), we obtain:

$$\frac{k_f}{k_{f0}} = \left( \frac{\phi_f}{\phi_{f0}} \right)^3 = \left( 1 + \frac{\alpha}{\phi_{f0}} \left( -\frac{1}{K_f} (\Delta \bar{\sigma} - \alpha_f \Delta p_f) + (\Delta \epsilon_{mb} - \Delta \epsilon_{ma}) + \frac{\Delta p_f}{K_m} \right) \right)^3 \tag{14}$$

Under our experimental condition, if we choose the time that the applied confining pressure and gas pressure is constant as the initial state ( $\Delta \bar{\sigma} = 0, \Delta p_f = 0$ ), then the permeability ratio can be defined as

$$\frac{k_f}{k_{f0}} = \left( \frac{\phi_f}{\phi_{f0}} \right)^3 = \left( 1 + \frac{\alpha}{\phi_{f0}} (\Delta \epsilon_{mb}(t) - \Delta \epsilon_{ma}(t)) \right)^3 \tag{15}$$

We set the f2 face to be a symmetric boundary and use the modelling strain results of M1 close to the fracture, and M7 distant from the fracture, as the selected strain points, to calculate the evolution of fracture permeability ratio according to the non-uniform strain model. As shown in Fig. 12, the modelling results demonstrate that the fracture permeability ratio recovered from the aperture model (Eq. 6) is in good agreement with the laboratory results, according to the non-uniform strain model (Eq. 15).

Under reservoir conditions, these stress gradients transfers exist at different scales—from natural fractures to those produced as a result of hydraulic fracturing. Thus, there is a complex series of interactions between these systems at different scales. For reservoir samples, the adsorption capacity is much larger than that of outcrop samples, and there is a high pore pressure change during shale gas extraction, that determines the aperture evolution of the fracture at different scales (include micro- and macro-natural fractures and hydraulic fractures) during gas extraction (e.g., CH<sub>4</sub>) or injection (e.g., CO<sub>2</sub>), which could affect the long-term production.

## 5 Conclusions

In this study, we measured and analyzed the evolution of strain gradients in a prismatic sample of shale during gas injection to determine processes controlling the evolution of strain gradients—from the initial state to ultimate equilibrium. These observations were used to estimate the influence of strain on fracture permeability evolution. The following conclusions can be drawn:

- Experimental results show that the observed sorption-induced strain gradients are inconsistent with the assumptions of conventional dual-porosity models. Under the non-equilibrium condition, the swelling of the matrix near fractures not only leads to the compaction

and narrowing of fractures but also shrinks the matrix away from the fracture, for the constant confining pressure condition.

- The time to reach the minimum linear strain and the magnitude of the minimum linear strain is closely related to the distances (of the strain gauges) from the fracture. The time to reach this minimum linear strain increases gradually with an increase in the distance from the strain gauges to the fracture. The shale matrix exhibits a cer-

**Fig. 11** Illustration of the definition of fracture strain (Wei et al. 2019a)

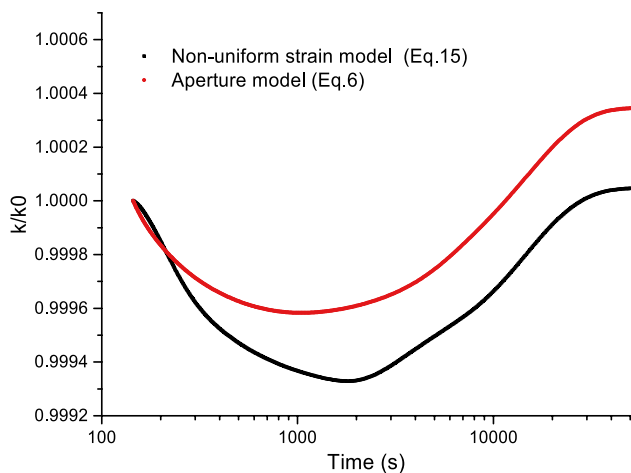
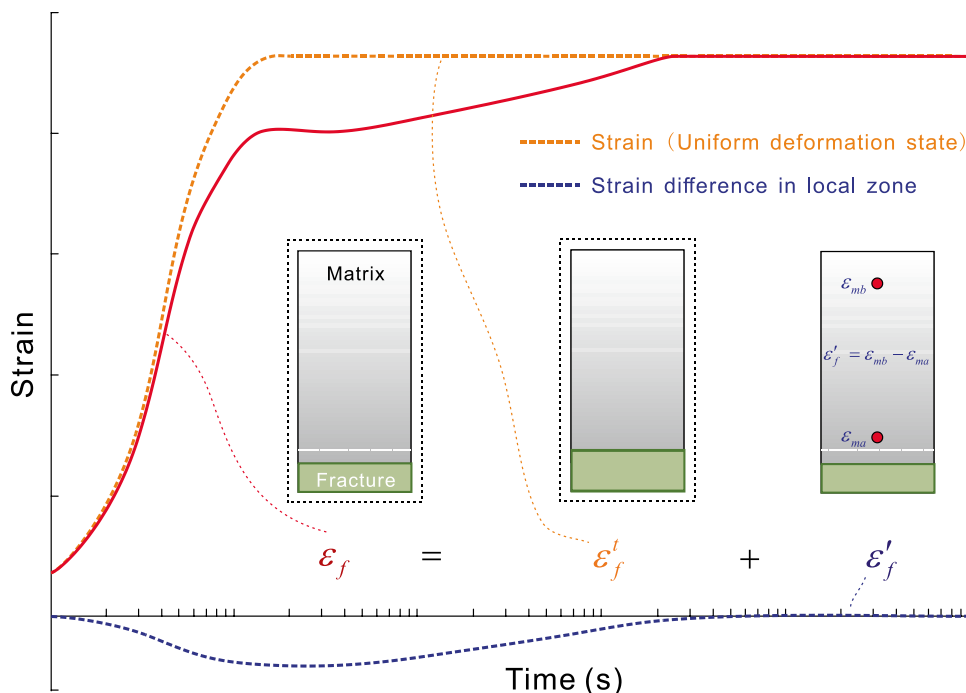


**Fig. 12** Comparison between different model results for fracture permeability ratio

tain degree of heterogeneity, and this heterogeneity might influence the magnitude of the minimum linear strain which is not proportional to the distances of the strain gauges from the fracture.

- The matrix strain gradients are determined by the matrix–fracture interactions during the experiment before equilibrium. Furthermore, the evolution of fracture permeability is influenced by matrix–fracture interactions and can be quantitatively characterized through a non-uniform strain component in the matrix.

**Acknowledgements** This work was funded by the Natural Science Foundation of China (41972184), the Fund of Outstanding Talents in Discipline of China University of Geosciences (Wuhan) (102-162301192664), the Natural Science Foundation of Hebei Province (E2020209074), and the Fundamental Research Funds for National Universities, China University of Geosciences (Wuhan). These supports are gratefully acknowledged.

**Declarations**

**Conflict of Interest** The authors declare that they have no conflict of interest.

**Research Highlights** A dense array of strain gauges is used to constrain the complex evolution of strain in shales containing a fracture. Complex transient and non-uniform strains develop as a result of even uniform confining stress. These strain gradients suggest a heterogeneous evolution of fracture permeability that can be rationalized from the mechanics of deformation.

**References**

Aljamaan H, Alnoaimi K, Kovscek A (2013) In-depth experimental investigation of shale physical and transport properties. In: Paper presented at the In: Unconventional Resources Technology Conference, Denver, Colorado, USA,  
 Alnoaimi K, Kovscek A (2013) Experimental and numerical analysis of gas transport in shale including the role of sorption. In: Paper presented at the In: SPE Annual Technical Conference and Exhibition, New Orleans, Louisiana, USA, 30 September-2 October  
 Alnoaimi KR, Duchateau C, Kovscek (2014) A Characterization and measurement of multi-scale gas transport in shale core samples.

- In: Unconventional Resources Technology Conference, Denver, Colorado, USA, 25–27 August 2014. pp 1–19. <https://doi.org/10.15530/urtec-2014-1920820>
- Chen T, Feng X-T, Cui G, Tan Y, Pan Z (2019) Experimental study of permeability change of organic-rich gas shales under high effective stress. *J Nat Gas Sci Eng* 64:1–14
- Chen Y, Jiang C, Yin G, Wojtanowicz AK, Zhang D (2020) Permeability and effective stress in dipping gas shale formation with bedding—experimental study. *J Energy Resour Technol* 142
- Cui XA, Bustin RM, Brezovski R, Nassichuk B, Glover K, Pathi V (2010) A new method to simultaneously measure in-situ permeability and porosity under reservoir conditions: implications for characterization of unconventional gas reservoirs. In: Canadian Unconventional Resources and International Petroleum Conference, Calgary, Alberta, Canada, 2010. pp 1–8. <https://doi.org/10.2118/138148-MS>
- Cui G, Liu J, Wei M, Feng X, Elsworth D (2018a) Evolution of permeability during the process of shale gas extraction. *J Nat Gas Sci Eng* 49:94–109
- Cui G, Liu J, Wei M, Shi R, Elsworth D (2018b) Why shale permeability changes under variable effective stresses: new insights. *Fuel* 213:55–71. <https://doi.org/10.1016/j.fuel.2017.10.068>
- Fan C, Elsworth D, Li S, Zhou L, Yang Z, Song Y (2019) Thermo-hydro-mechanical-chemical couplings controlling CH<sub>4</sub> production and CO<sub>2</sub> sequestration in enhanced coalbed methane recovery. *Energy* 173:1054–1077
- Fink R, Krooss BM, Gensterblum Y, Amann-Hildenbrand A (2017) Apparent permeability of gas shales—superposition of fluid-dynamic and poro-elastic effects. *Fuel* 199:532–550
- Firouzi M, Alnoaimi K, Kovscek A, Wilcox J (2014) Klinkenberg effect on predicting and measuring helium permeability in gas shales. *Int J Coal Geol* 123:62–68. <https://doi.org/10.1016/j.coal.2013.09.006>
- Florence FA, Rushing J, Newsham KE, Blasingame TA (2007) Improved permeability prediction relations for low permeability sands. In: Rocky Mountain Oil and Gas Technology Symposium, Denver, Colorado, USA, 16–18 April 2007. pp 1–18. <https://doi.org/10.2118/107954-MS>
- Gallé C (2001) Effect of drying on cement-based materials pore structure as identified by mercury intrusion porosimetry: a comparative study between oven-, vacuum-, and freeze-drying. *Cem Concr Res* 31:1467–1477
- Gan H, Nandi S, Walker P Jr (1972) Nature of the porosity in American coals. *Fuel* 51:272–277
- Gao J, Yu Q (2018) Effect of Water Saturation on Pressure-Dependent Permeability of Carboniferous Shale of the Qaidam Basin, China. *Transp Porous Media* 123:147–172. <https://doi.org/10.1007/s11242-018-1029-y>
- Ghanizadeh A, Amann-Hildenbrand A, Gasparik M, Gensterblum Y, Krooss BM, Littke R (2014) Experimental study of fluid transport processes in the matrix system of the European organic-rich shales: II. Posidonia Shale (Lower Toarcian, northern Germany). *Int J Coal Geol* 123:20–33
- Guo F (2014) Experimental Investigation of Shale Permeability. The University of Western Australia
- He B, Xie L, Zhao P, Ren L, Zhang Y (2020) Highly efficient and simplified method for measuring the permeability of ultra-low permeability rocks based on the pulse-decay technique. *Rock Mech Rock Eng* 53:291–303
- Heller R, Vermilyen J, Zoback M (2014) Experimental investigation of matrix permeability of gas shales. *AAPG Bull* 98:975–995. <https://doi.org/10.1306/09231313023>
- Hu Q, Ewing RP, Rowe HD (2015) Low nanopore connectivity limits gas production in Barnett formation. *J Geophys Res* 120:8073–8087
- Jin G, Pérez HG, Agrawal G, Khodja MR, Ali AZ, Hussaini SR, Jangda ZZ (2015) The impact of gas adsorption and composition on unconventional shale permeability measurement. In: SPE Middle east oil and gas show and conference, Manama, Bahrain, 8–11 March 2015. pp 1–13. <https://doi.org/10.2118/172744-MS>
- Kang Y, Chen M, Li X, You L, Yang B (2015) Laboratory measurement and interpretation of nonlinear gas flow in shale. *Int J Mod Phys C* 26:1550063. <https://doi.org/10.1142/S0129183115500631>
- Karacan CÖ (2007) Swelling-induced volumetric strains internal to a stressed coal associated with CO<sub>2</sub> sorption. *Int J Coal Geol* 72:209–220
- Karacan CÖ, Ruiz FA, Cotè M, Phipps S (2011) Coal mine methane: a review of capture and utilization practices with benefits to mining safety and to greenhouse gas reduction. *Int J Coal Geol* 86:121–156
- Katz A, Thompson A (1986) Quantitative prediction of permeability in porous rock. *Phys Rev B* 34:8179
- Kiyama T, Nishimoto S, Fujioka M, Xue Z, Ishijima Y, Pan Z, Connell LD (2011) Coal swelling strain and permeability change with injecting liquid/supercritical CO<sub>2</sub> and N<sub>2</sub> at stress-constrained conditions. *Int J Coal Geol* 85:56–64
- Klinkenberg L (1974) The permeability of porous media to liquids and gases. In: *Drilling and production practice*, New York, USA, pp 200–213.
- Kumar H, Elsworth D, Mathews J, Marone C (2016) Permeability evolution in sorbing media: analogies between organic-rich shale and coal. *Geofluids* 16:43–55. <https://doi.org/10.1111/gff.12135>
- Letham EA (2011) Matrix permeability measurements of gas shales: gas slippage and adsorption as sources of systematic. Error. <https://doi.org/10.14288/1.0053604>
- Li X, Feng Z, Han G, Elsworth D, Marone C, Saffer D, Cheon D-S (2017) Permeability evolution of propped artificial fractures in green river shale. *Rock Mech Rock Eng* 50:1473–1485. <https://doi.org/10.1007/s00603-017-1186-2>
- Li W, Liu J, Zeng J, Leong Y-K, Elsworth D, Tian J, Li L (2020) A fully coupled multidomain and multiphysics model for evaluation of shale gas extraction. *Fuel* 278:118214
- Liu S, Harpalani S (2013) A new theoretical approach to model sorption-induced coal shrinkage or swelling. *AAPG Bull* 97:1033–1049
- Liu S, Harpalani S (2014) Determination of the effective stress law for deformation in coalbed methane reservoirs. *Rock Mech Rock Eng* 47:1809–1820
- Liu J, Chen Z, Elsworth D, Miao X, Mao X (2010) Evaluation of stress-controlled coal swelling processes. *Int J Coal Geol* 83:446–455
- Liu J, Chen Z, Elsworth D, Qu H, Chen D (2011) Interactions of multiple processes during CBM extraction: a critical review. *Int J Coal Geol* 87:175–189. <https://doi.org/10.1016/j.coal.2011.06.004>
- Liu S, Wang Y, Harpalani S (2016) Anisotropy characteristics of coal shrinkage/swelling and its impact on coal permeability evolution with CO<sub>2</sub> injection. *Greenhouse Gases Sci Technol* 6:615–632
- Liu X, Sheng J, Liu J, Hu Y (2018) Evolution of coal permeability during gas injection—from initial to ultimate equilibrium. *Energies* 11(10):2800
- Liu T, Lin B, Fu X, Gao Y, Kong J, Zhao Y, Song H (2020) Experimental study on gas diffusion dynamics in fractured coal: a better understanding of gas migration in in-situ coal seam. *Energy* 195:117005
- Lomize G (1951) Flow in fractured rocks. *Gosenergoizdat Moscow* 127:635
- Ma Y, Pan Z, Zhong N, Connell LD, Down DI, Lin W, Zhang Y (2016) Experimental study of anisotropic gas permeability and its relationship with fracture structure of Longmaxi Shales, Sichuan Basin, China. *Fuel* 180:106–115

- McKernan R, Rutter E, Mecklenburgh J, Taylor K, Covey-Crump S (2014) Influence of effective pressure on mudstone matrix permeability: implications for shale gas production. In: SPE/EAGE European Unconventional Resources Conference and Exhibition, 2014. vol 1. European Association of Geoscientists and Engineers, pp 1–13
- Moghadam AA, Chalaturnyk R (2015) Laboratory investigation of shale permeability. In: SPE/CSUR Unconventional Resources Conference, Calgary, Alberta, Canada., pp 1–27. <https://doi.org/10.2118/175919-MS>
- Moghadam AA, Chalaturnyk R (2016) Analytical and experimental investigations of gas-flow regimes in shales considering the influence of mean effective stress. *SPE J* 21:557–572. <https://doi.org/10.2118/178429-PA>
- Moghaddam RN, Jamiolahmady M (2016) Fluid transport in shale gas reservoirs: Simultaneous effects of stress and slippage on matrix permeability. *Int J Coal Geol* 163:87–99. <https://doi.org/10.1016/j.coal.2016.06.018>
- Pan Z, Connell LD (2007) A theoretical model for gas adsorption-induced coal swelling. *Int J Coal Geol* 69:243–252
- Pan Z, Ma Y, Danesh NN, Connell LD, Sander R, Down DI, Camilleri M (2015a) Measurement of shale anisotropic permeability and its impact on shale gas production. In: SPE Asia Pacific Unconventional Resources Conference and Exhibition, Society of Petroleum Engineers,
- Pan Z, Ma Y, Danesh NN, Connell LD, Sander R, Down DI, Camilleri M (2015b) Measurement of shale anisotropic permeability and its impact on shale gas production. In: SPE Asia Pacific Unconventional Resources Conference and Exhibition, Brisbane, Australia, pp 1–15. <https://doi.org/10.2118/176955-MS>
- Peng S, Loucks B (2016) Permeability measurements in mudrocks using gas-expansion methods on plug and crushed-rock samples. *Mar Pet Geol* 73:299–310
- Ren Y, Guo X, Xie C, Wu H (2016) Experimental study on gas slippage of Marine Shale in Southern China. *Petroleum* 2:171–176. <https://doi.org/10.1016/j.petlm.2016.03.003>
- Sander R, Pan Z, Connell LD (2017) Laboratory measurement of low permeability unconventional gas reservoir rocks: a review of experimental methods. *J Nat Gas Sci Eng* 37:248–279. <https://doi.org/10.1016/j.jngse.2016.11.041>
- Sang G, Elsworth D, Miao X, Mao X, Wang J (2016) Numerical study of a stress dependent triple porosity model for shale gas reservoirs accommodating gas diffusion in kerogen. *J Nat Gas Sci Eng* 32:423–438
- Sang G, Elsworth D, Liu S, Harpalani S (2017) Characterization of swelling modulus and effective stress coefficient accommodating sorption-induced swelling in coal. *Energy Fuels* 31:8843–8851
- Shen Y, Pang Y, Shen Z, Tian Y, Ge H (2018) Multiparameter analysis of gas transport phenomena in shale gas reservoirs: apparent permeability characterization. *Sci Rep* 8:2601. <https://doi.org/10.1038/s41598-018-20949-2>
- Shi R, et al. (2020) Experimental observations of heterogeneous strains inside a dual porosity sample under the influence of gas-sorption: a case study of fractured coal. *Int J Coal Geol*:103450
- Shi R, Liu J, Wei M, Elsworth D, Wang X (2018) Mechanistic analysis of coal permeability evolution data under stress-controlled conditions. *Int J Rock Mech Min Sci* 110:36–47. <https://doi.org/10.1016/j.ijrmms.2018.07.003>
- Tan Y, Pan Z, Liu J, Wu Y, Haque A, Connell LD (2017) Experimental study of permeability and its anisotropy for shale fracture supported with proppant. *J Nat Gas Sci Eng* 44:250–264
- Tan Y, Pan Z, Liu J, Feng X-T, Connell LD (2018) Laboratory study of proppant on shale fracture permeability and compressibility. *Fuel* 222:83–97
- Tan Y, Pan Z, Feng X-T, Zhang D, Connell LD, Li S (2019) Laboratory characterisation of fracture compressibility for coal and shale gas reservoir rocks: a review. *Int J Coal Geol* 204:1–17
- van Noort R, Yarushina V (2019) Water, CO<sub>2</sub> and argon permeabilities of intact and fractured shale cores under stress. *Rock Mech Rock Eng* 52:299–319
- Wang Q, Chen X, Jha AN, Rogers H (2014) Natural gas from shale formation—the evolution, evidences and challenges of shale gas revolution in United States. *Renew Sustain Energy Rev* 30:1–28
- Wang C, Liu J, Feng J, Wei M, Wang C, Jiang Y (2016) Effects of gas diffusion from fractures to coal matrix on the evolution of coal strains: Experimental observations. *Int J Coal Geol* 162:74–84
- Wang X, Zhu Y, Fu C (2019) Experimental investigation of the stress-dependent permeability in the Longmaxi Formation shale. *J Pet Sci Eng* 175:932–947
- Washburn EW (1921) The dynamics of capillary flow. *Phys Rev* 17:273
- Wei M, Liu J, Feng X, Wang C, Zhou F (2016) Evolution of shale apparent permeability from stress-controlled to displacement-controlled conditions. *J Nat Gas Sci Eng* 34:1453–1460. <https://doi.org/10.1016/j.jngse.2016.07.012>
- Wei M, Liu Y, Liu J, Elsworth D, Zhou F (2019) Micro-scale investigation on coupling of gas diffusion and mechanical deformation of shale. *J Pet Sci Eng* 175:961–970
- Wei M, Liu J, Elsworth D, Li S, Zhou F (2019) Influence of gas adsorption induced non-uniform deformation on the evolution of coal permeability. *Int J Rock Mech Min Sci* 114:71–78
- Wei M, Liu J, Elsworth D, Liu Y, Zeng J, He Z (2021) Impact of equilibration time lag between matrix and fractures on the evolution of coal permeability. *Fuel* 290:120029
- Werner AK, Vink S, Watt K, Jagals P (2015) Environmental health impacts of unconventional natural gas development: a review of the current strength of evidence. *Sci Total Environ* 505:1127–1141
- Wildenschild D, Sheppard AP (2013) X-ray imaging and analysis techniques for quantifying pore-scale structure and processes in subsurface porous medium systems. *Adv Water Resour* 51:217–246
- Wu Y, Liu J, Elsworth D, Chen Z, Connell L, Pan Z (2010) Dual poroelastic response of a coal seam to CO<sub>2</sub> injection. *Int J Greenh Gas Control* 4:668–678
- Wu Y, Liu J, Chen Z, Elsworth D, Pone D (2011) A dual poroelastic model for CO<sub>2</sub>-enhanced coalbed methane recovery. *Int J Coal Geol* 86:177–189
- Yang Y, Liu S (2019) Estimation and modeling of pressure-dependent gas diffusion coefficient for coal: a fractal theory-based approach. *Fuel* 253:588–606
- Zamirian M, Aminian KK, Ameri S, Fathi E (2014a) New steady-state technique for measuring shale core plug permeability. In: SPE/CSUR Unconventional Resources Conference—Canada, Calgary, Alberta, Canada, pp 1–11. <https://doi.org/10.2118/171613-MS>
- Zamirian M, Aminian KK, Ameri S, Fathi E (2014b) New steady-state technique for measuring shale core plug permeability. In: SPE/CSUR unconventional resources conference—canada, Society of Petroleum Engineers
- Zeng J, Liu J, Li W, Leong Y-K, Elsworth D, Guo J (2020) Evolution of shale permeability under the influence of gas diffusion from the fracture wall into the matrix. *Energy Fuels* 34:4393–4406
- Zhang H, Liu J, Elsworth D (2008) How sorption-induced matrix deformation affects gas flow in coal seams: a new FE model. *Int J Rock Mech Min Sci* 45:1226–1236
- Zhao Y, Wang C, Zhang Y, Liu Q (2019) Experimental study of adsorption effects on shale permeability. *Nat Resour Res* 28:1575–1586
- Zhou J, Liu G, Jiang Y, Xian X, Liu Q, Zhang D, Tan J (2016) Supercritical carbon dioxide fracturing in shale and the coupled effects on the permeability of fractured shale: an experimental study. *J Nat Gas Sci Eng* 36:369–377. <https://doi.org/10.1016/j.jngse.2016.10.005>

Zhou J, Zhang L, Li X, Pan Z (2019) Experimental and modeling study of the stress-dependent permeability of a single fracture in shale under high effective stress. *Fuel* 257:116078

Zhou J et al (2020) Experimental investigation on the influence of sub-and super-critical CO<sub>2</sub> saturation time on the permeability of fractured shale. *Energy* 191:116574

Zhu W, Tian W, Gao Y, Deng J, Zhang X, Qi Q, Ma Q (2016) Study on experiment conditions of marine shale gas seepage law. *J Nat Gas Geosci* 1:157–163. <https://doi.org/10.1016/j.jnggs.2016.05.006>

**Publisher's Note** Springer Nature remains neutral with regard to jurisdictional claims in published maps and institutional affiliations.